

# Magnetic Order and Spin Dynamics in Ferroelectric $\text{HoMnO}_3$

O. P. Vajk,<sup>1</sup> M. Kenzelmann,<sup>1,2</sup> J. W. Lynn,<sup>1</sup> S. B. Kim,<sup>3</sup> and S.-W. Cheong<sup>3</sup>

<sup>1</sup>NIST Center for Neutron Research, Gaithersburg, MD 20899

<sup>2</sup>Department of Physics and Astronomy, Johns Hopkins University, Baltimore, MD 21218

<sup>3</sup>Department of Physics and Astronomy, Rutgers University, Piscataway, New Jersey 08854

(Dated: November 18, 2021)

Hexagonal  $\text{HoMnO}_3$  is a frustrated antiferromagnet ( $T_N=72$  K) ferroelectric ( $T_C=875$  K) in which these two order parameters are coupled. Our neutron measurements of the spin wave dispersion for the  $S = 2$   $\text{Mn}^{3+}$  on the layered triangular lattice are well described by a two-dimensional nearest-neighbor Heisenberg exchange  $J=2.44$  meV, and an anisotropy  $D$  that is 0.093 meV above the spin reorientation transition at 40 K, and 0.126 meV below. For  $H \parallel c$  the magnetic structures and phase diagram have been determined, and reveal additional transitions below 8 K where the ferroelectrically displaced  $\text{Ho}^{3+}$  ions are ordered magnetically.

PACS numbers: 75.30.Ds, 75.30.Et, 75.50.Ee

Magnetic ferroelectric materials are rare, and rarer still are systems where these two disparate order parameters exhibit significant coupling [1]. Such multiferroics have been of particular interest recently both to understand the fundamental aspects of this coupling [2, 3, 4, 5, 6], and because of the intriguing possibility of using these coupled order parameters in novel device applications [7]. The hexagonal  $\text{HoMnO}_3$  system of particular interest here is a prototype multiferroic where the Ho-O displacements give rise to a ferroelectric moment ( $T_C = 875$  K) along the  $c$ -axis, the Mn moments order at 72 K, and the order parameters are naturally coupled through the Ho-Mn exchange and anisotropy interactions. The magnetic system has the added interest that the Mn moments occupy a fully frustrated triangular lattice. Our inelastic neutron scattering measurements of the Mn spin dynamics reveal the planar nature of the spin system, and allow us to establish the basic model for the magnetic interactions in the system and determine the interaction parameters. Field-dependent neutron diffraction measurements reveal the nature of the magnetic phase diagram, and in particular the Ho involvement in the hysteretic magnetic transitions at low temperatures. Our results also suggest that the Ho coupling may be responsible for the first-order spin-flop transition found at intermediate temperatures.

We have grown single crystals of  $\text{HoMnO}_3$  using a traveling solvent optical floating zone furnace, and the diffraction and inelastic neutron measurements were performed at the NIST Center for Neutron Research on the BT2 and BT9 thermal triple-axis instruments. The magnetic structure of  $\text{HoMnO}_3$  has been studied previously with neutron powder diffraction [8, 9, 10], optical second-harmonic generation (SHG) [11, 12, 13, 14], and magnetic and dielectric susceptibility [2]. The  $\text{Mn}^{3+}$  ions are arranged in a 2-dimensional (2D) triangular lattice, with successive layers offset from each other. Fig. 1 shows the integrated intensities of the (1,0,0) and (1,0,1) (commensurate) magnetic Bragg peaks, where we see that below  $T_N \approx 72$  K the spin-2  $\text{Mn}^{3+}$  moments order antiferromagnetically in a non-collinear 120-degree structure

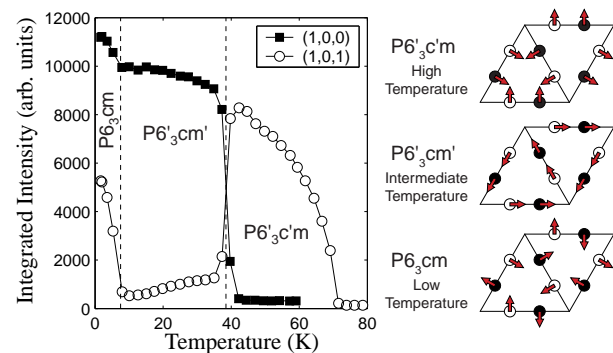


FIG. 1: (color online). Neutron diffraction measurements of the (1,0,0) and (1,0,1) magnetic Bragg reflection integrated intensity. Two spin reorientation transitions (indicated by dashed lines) lead to changes in the intensities of both peaks. The  $\text{Mn}^{3+}$  spin configurations for these phases are shown in the schematics to the right, where open circles indicate the position of Mn ions at  $z = 0$ , filled circles indicate Mn ions at  $z = c/2$ , and arrows indicate the direction of the local magnetic moment.  $\text{Ho}^{3+}$  moments (not shown) order in the low-temperature phase.

within each plane. At  $T_{SR} \approx 40$  K a sharp spin reorientation transition is observed associated with a change in the magnetic symmetry to the  $P6'_3cm'$  structure, as indicated in Fig. 1. Below 8 K half of the  $\text{Ho}^{3+}$  moments order [9, 10], which results in a third zero-field spin reorientation transition of the Mn spins. The three zero-field Mn spin structures are also shown in Fig. 1.

Measurements of the spin-wave dispersion were performed on a 1.8 gram single crystal in both the (H,K,0) and (H,0,L) scattering planes. An example of a constant-Q scan at 20 K showing two distinct magnetic modes is shown in Fig. 2a. Fits to individual scans were used to establish the peak positions. The dispersion relations at 20 K, in the intermediate-temperature phase, are plotted in Fig. 2b and 2c along two different directions in reciprocal space. Data for the spin-wave dispersion along the (1,0,L) direction (inset Fig. 2c) show no discernible dispersion in the out-of-plane direction, indicating pri-

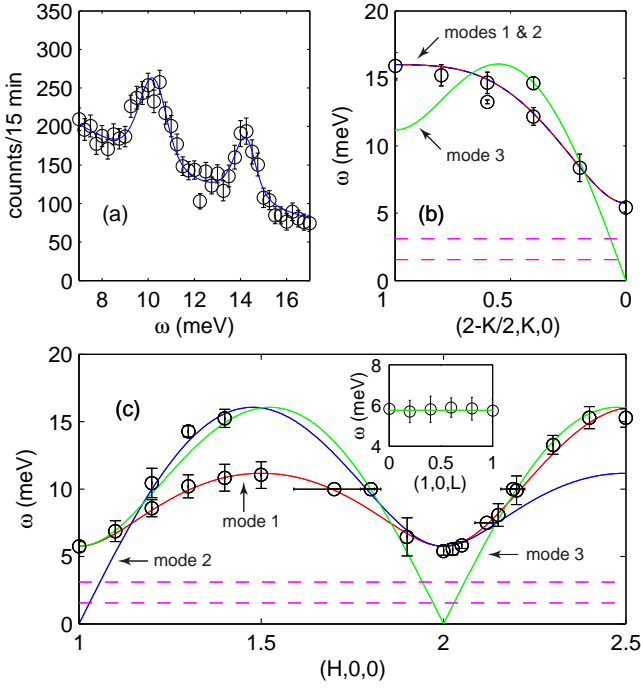


FIG. 2: (color online). Spin-wave dispersion at 20K. (a) Measurements of the spin waves at  $Q=(1.3,0,0)$ . Data were taken on BT2 with horizontal collimations of  $60^\circ\text{-}40^\circ\text{-}40^\circ\text{-}80^\circ$  and a fixed final energy of 14.7 meV. The line shows a fit to the data using two modes convoluted with the resolution function. Peak positions from both constant-energy and constant- $Q$  scans are plotted for two in-plane directions in reciprocal space in (b) and (c), along with the three modes of the dispersion curve (solid lines) given by Eq. 4 ( $J = 2.44(7)$  meV and  $D = 0.126(25)$  meV). Dashed lines indicate two (dispersionless) crystal field levels of Ho at 1.5(1) and 3.1(1) meV. Inset: L dependence of the spin-wave spectrum, showing no discernable dispersion.

marily 2D spin dynamics. Data were also taken at 50K, in the high-temperature phase, and a comparison of two constant- $Q$  scans at the magnetic zone center are shown in Fig. 3a. The zone-center gap decreases significantly, as shown in the comparison of the 20K and 50K dispersion data in Fig. 3b.

The dispersion of the excitations in  $\text{HoMnO}_3$  was calculated using a linear spin-wave analysis. We start from the Hamiltonian

$$H = J \sum_{\langle i,j \rangle} \mathbf{S}_i \cdot \mathbf{S}_j + D \sum_i S_i^z S_i^z, \quad (1)$$

where  $\langle i,j \rangle$  indicates the sum is over nearest-neighbor in-plane pairs,  $J$  is the primary antiferromagnetic exchange, and  $D$  is the anisotropy. Introducing three different flavors of bosons and using a Holstein-Primakoff transformation, we derive a linearized Hamiltonian which we diagonalize by mapping to the Hamiltonian of the quadratic quantum mechanical oscillator, similarly to Ref

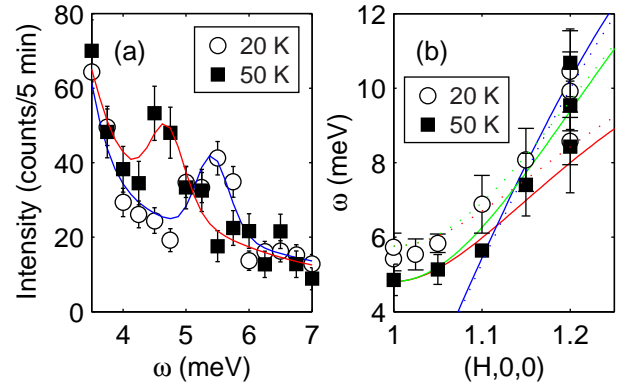


FIG. 3: (color online). (a) Inelastic neutron measurements at  $Q=(2,0,0)$  at 20K and 50K. Data were taken on BT9 with horizontal collimations of  $40^\circ\text{-}40^\circ\text{-}40^\circ\text{-}40^\circ$  and fixed incident energy of 13.7 meV. Lines show fits to the data. The increase in intensity at lower energies is primarily due to a crystal field excitation at 3.1 meV. (b) Comparison of 20K and 50K dispersion data near the zone center. Data have been reduced to the first Brillouin zone. Dotted lines show spin-wave dispersion curves for 20K data, as in Fig. 2. Solid lines show fit to 50K data ( $J = 2.44$  meV is fixed and  $D = 0.093(10)$  meV).

[15]. We define the lattice Fourier sum as

$$z = \frac{1}{12} \left\{ e^{-2\pi i(H/3-K/3)} + e^{2\pi i(2H/3+K/3)} + e^{-2\pi i(H/3+2K/3)} \right\}. \quad (2)$$

For simplicity, we now define

$$\begin{aligned} z_1 &= z + z^* \\ z_2 &= -(z + z^*)/2 + i(\sqrt{3}/2)(z - z^*) \\ z_3 &= -(z + z^*)/2 - i(\sqrt{3}/2)(z - z^*). \end{aligned} \quad (3)$$

We obtain three modes whose dispersion is given by

$$\omega_i = 3SJ\sqrt{(1 + 4z_i + 2D/J)(1 - 2z_i)}, \quad (4)$$

where  $i = 1, 2$ , or  $3$ , and  $S = 2$  is the spin at the  $\text{Mn}^{3+}$  ion. Equation 4 was used to fit our data, with the results shown by the curves in Figs. 2b, 2c, and 3b. This simple model provides a remarkably good description of the spin dynamics. Quantitatively, we obtain  $J = 2.44(7)$  meV and  $D = 0.126(25)$  at 20 K. Data taken away from the zone center showed little temperature dependence, while at the zone center there was a significant difference between the 20K and 50K data, indicating that the temperature dependence of the spin-wave spectrum comes largely from changes in the anisotropy. For the 50K data,  $J$  was therefore kept fixed at 2.44 meV, yielding  $D = 0.093(10)$ . The increase in the anisotropy  $D$  at lower temperatures is significant, and suggests that this anisotropy, likely originating from the holmium, drives the spin reorientation transition.

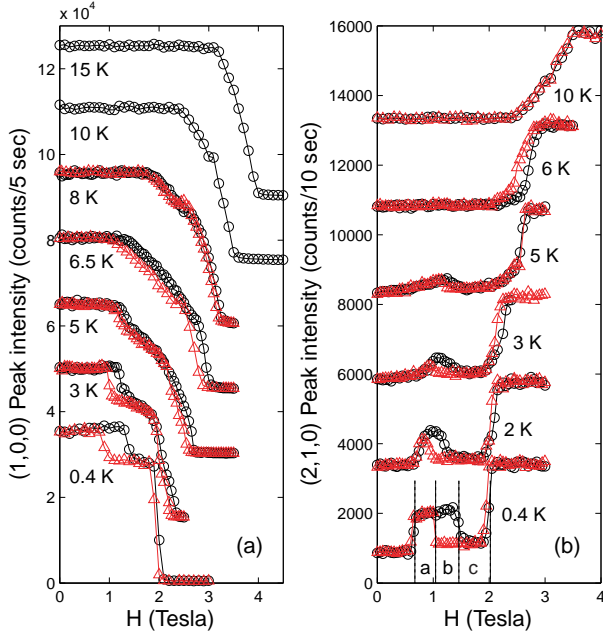


FIG. 4: (color online). (a) (1,0,0) magnetic Bragg peak intensity versus magnetic field for different temperatures (offset by 15,000 counts for clarity). (b) (2,1,0) magnetic Bragg peak intensity versus magnetic field for different temperatures. Circles are data taken with increasing field, while triangles are data taken with decreasing field. Dashed lines show 0.4K transitions, with two intermediate phases *a* and *c* and hysteretic overlap in region *b*.

In the presence of a magnetic field  $T_{SR}$  shifts to lower  $T$  and broadens, and  $\text{HoMnO}_3$  develops a reentrant  $P6_3c'm$  phase. A sharp anomaly in the dielectric susceptibility at  $T_{SR}$  indicates a coupling between the magnetic and ferroelectric order [5]. SHG measurements as a function of magnetic field also show the change in magnetic symmetry and the reentrant phase as a function of magnetic field suggested by dielectric susceptibility [13]. More recent measurements show a marked decrease in the strength of the SHG signal (which is due to the magnetic ordering of the  $\text{Mn}^{3+}$  ions) when an electric field is applied [6].

To investigate the magnetic field-dependent phase diagram, a 0.5 gram sample was mounted in the (H,K,0) scattering plane inside a vertical-field 7 Tesla superconducting magnet with a Helium-3 insert. A magnetic field of up to 5 Tesla was applied along the  $c$  axis, and the (commensurate) (1,0,0) and (2,1,0) magnetic peaks were used to track the evolution of the magnetic phases with magnetic field and temperature. In the intermediate temperature phase, a sufficiently strong applied magnetic field along the  $c$  axis pushes  $\text{HoMnO}_3$  into the high-temperature phase [5, 13]. The boundary between the intermediate- and high-temperature phases (shown in Fig. 5 as a function of temperature and magnetic field) is in agreement with the phase diagram established from dielectric susceptibility measurements [5, 16].

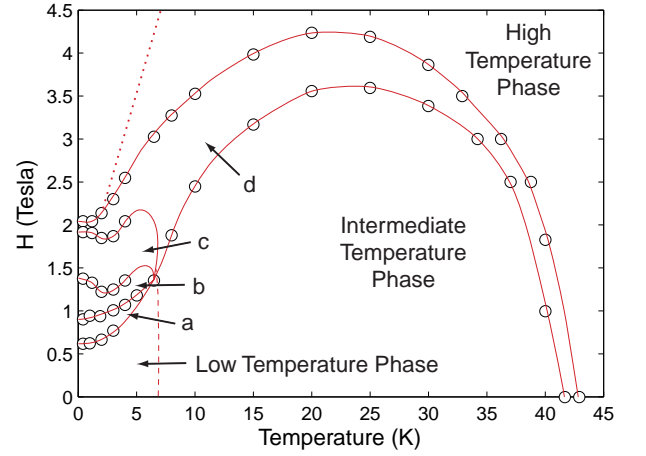


FIG. 5: (color online). Temperature and magnetic field phase diagram for  $\text{HoMnO}_3$  obtained from diffraction measurements of the (1,0,0) and (2,1,0) Bragg reflections. Lines are guides to the eye. Regions *a* and *c* are intermediate phases, with hysteretic overlap in region *b*, as in Fig. 4. Region *d* is an intermediate region where peak intensities change continuously. Dashed line is approximate location of low-temperature  $\text{Ho}^{3+}$  ordering transition, and dotted line is approximate transition observed by SHG and magnetic susceptibility measurements [13, 16]. These transitions were not observable from the (1,0,0) and (2,1,0) diffraction data.

At lower temperatures the transition becomes considerably more complicated. Figure 4a shows the peak intensity of the (1,0,0) Bragg scattering as a function of magnetic field at several temperatures. At higher temperatures, the intensity decreases approximately linearly with increasing field over a well-defined transition region. At 0.4K, however, there are two distinct, step-like transitions, with considerable hysteresis in the lower-field transition, indicating the existence of a well-defined intermediate phase between the low- and high-field phases. As the temperature increases, these transitions become broader and the hysteresis decreases, merging together into the single transition (without appreciable hysteresis) observable at higher temperatures.

Figure 4b shows equivalent measurements of the (2,1,0) Bragg peak intensity. Again, at high temperatures, an approximately linear change in scattering intensity over a well-defined transition region is observable. At low temperatures, as for the (1,0,0) reflection, the situation becomes more complicated. Instead of two, we find three transitions, with an additional lower-field transition not observable in the (1,0,0) data. Unlike the (1,0,0) reflection, the scattering intensity of the (2,1,0) reflection does not change monotonically.

Figure 5 shows a phase diagram extracted from the (1,0,0) and (2,1,0) diffraction data. Below 4K there are two distinct intermediate phases (labeled *a* and *b*) between the zero-field and high-field phases, with significant hysteretic overlap between them. These data are not sensitive to the low-temperature spin reorientation ob-

servable in the (2,1,0) diffraction data (Fig. 1), indicated roughly by the dashed line in Fig. 5. It is interesting to note, however, that the intermediate phases are only observable below the low-temperature spin reorientation transition where  $\text{Ho}^{3+}$  ordering becomes significant.

At higher temperatures, our phase diagram agrees well with previous dielectric measurements [5]. These SHG measurements did not observe any intermediate phase at low temperatures [13], while more recent magnetic susceptibility and heat capacity measurements have identified one intermediate phase [16]. While we observe two unambiguous, distinct intermediate phases at low temperatures, the combined intermediate phases we observe agree qualitatively with the intermediate phase recently observed [16]. Further measurements of out-of-plane magnetic peaks will be necessary in order to determine the exact magnetic structure of these intermediate phases. Recent SHG measurements suggest that  $\text{Ho}^{3+}$  magnetic moments can even be ordered ferromagnetically with the application of an electric field [6]. Neutron scattering reveals considerable complexity in the magnetic field phase diagram for  $\text{HoMnO}_3$ , and extending these neutron measurements to the electric field phase diagram may also prove similarly revealing.

The out-of-plane magnetic interactions in  $\text{HoMnO}_3$ , both between successive  $\text{Mn}^{3+}$  layers and between  $\text{Mn}^{3+}$  and  $\text{Ho}^{3+}$ , are almost completely frustrated. It is therefore not surprising that the spin dynamics in the intermediate and high temperature phases are two-dimensional in nature, and we find that the spin-wave spectrum is well described by Eq. 1. Ferroelectric lattice distortions relieve the interplane frustrations in  $\text{HoMnO}_3$  [6], and may be the driving force behind the spin-reorientation tran-

sitions of the  $\text{Mn}^{3+}$  magnetic lattice. The role of Ho in these reorientation transitions may be very similar to the role of Nd in  $\text{Nd}_2\text{CuO}_4$ , another layered transition-metal oxide in which frustrated interplanar interactions enable weak, higher-order interactions to dictate the magnetic structure.  $\text{Nd}_2\text{CuO}_4$  has a non-collinear structure [17] with Cu spin-reorientation transitions [18, 19] that are controlled by the rare earth single-ion anisotropy [20, 21]. We suggest that it is a similar interaction in  $\text{HoMnO}_3$  that controls the spin-flop transition, and is the origin of the magnetic-ferroelectric coupling.

There has been considerable experimental progress in recent years on mapping out the magnetic phase diagram of  $\text{HoMnO}_3$  and discovering signatures of the interplay of magnetic and ferroelectric order in various physical properties. However, a theoretical understanding of these interactions is still lacking. Although a complete theoretical description of  $\text{HoMnO}_3$  will necessarily require significantly more complexity than Eq. 1, having experimentally determined the dispersion relations and values for the primary magnetic exchange constants is an important step toward being able to model the interaction between ferroelectric and magnetic order in  $\text{HoMnO}_3$ .

#### Acknowledgments

Work at Rutgers was supported by NSF-MRSEC Grant No. DMR 00-80008. Work at NIST was supported in part by the Binational Science Foundation, Grant No. 2000073. MK was supported by the National Science Foundation through DMR-0306940. Data reduction was performed with DAVE software, supported by NSF Agreement No. DMR-0086210.

- 
- [1] N. A. Hill, J. Phys. Chem. B **104**, 6694 (2000).
  - [2] H. Sugie, N. Iwata, and K. Kohn, J. Phys. Soc. Jpn. **71**, 1558 (2002).
  - [3] T. Kimura, T. Goto, M. Shintani, K. Ishizaka, T. Arima, and Y. Tokura, Nature **426**, 55 (2003).
  - [4] N. Hur, S. Park, P. A. Sharma, J. S. Ahn, S. Guha, and S. Cheong, Nature **429**, 392 (2004).
  - [5] B. Lorenz, A. P. Litvinchuk, M. M. Gospodinov, and C. W. Chu, Phys. Rev. Lett. **92**, 087204 (2004).
  - [6] T. Lottermoser, T. Lonkai, U. Amann, D. Hohlwein, J. Ihringer, and M. Fiebig, Nature **430**, 541 (2004).
  - [7] H. Zheng *et al.*, Science **303**, 661 (2004).
  - [8] W. C. Koehler, H. L. Yakel, E. O. Wollan, and J. W. Cable, Phys. Lett. **9**, 93 (1964).
  - [9] A. Muñoz, J. A. Alonso, M. J. Martínez-Lope, M. T. Casáis, J. L. Martínez, and M. T. Fernández-Díaz, Chem. Mater. **13**, 1497 (2001).
  - [10] T. Lonkai, D. Hohlwein, J. Ihringer, and W. Prandl, Appl. Phys. A **74**, S843 (2002).
  - [11] M. Fiebig, D. Fröhlich, K. Kohn, S. Leute, T. Lottermoser, V. V. Pavlov, and R. V. Pisarev, Phys. Rev. Lett. **84**, 5620 (2000).
  - [12] M. Fiebig, D. Fröhlich, T. Lottermoser, and K. Kohn, Appl. Phys. Lett. **77**, 4401 (2000).
  - [13] M. Fiebig, C. Degenhardt, and R. V. Pisarev, J. Appl. Phys. **91**, 8867 (2002).
  - [14] M. Fiebig, D. Fröhlich, T. Lottermoser, and M. Maat, Phys. Rev. B **66**, 144102 (2002).
  - [15] A. B. Harris, C. Kallin, and A. J. Berlinsky, Phys. Rev. B **45**, 2899 (1992).
  - [16] B. Lorenz *et al.*, cond-mat/0408499.
  - [17] S. Skanthakumar, J. W. Lynn, J. L. Peng, and Z. Y. Li, Phys. Rev. B **47**, R6173 (1993).
  - [18] S. Skanthakumar, H. Zhang, T. W. Clinton, W. Li, J. W. Lynn, Z. Fisk, and S. Cheong, Physica C **160**, 124 (1989).
  - [19] Y. Endoh, M. Matsuda, K. Yamada, K. Kakurai, Y. Hidaka, G. Shirane, and R. J. Birgeneau, Phys. Rev. B **40**, 7023 (1989).
  - [20] R. Sachidanandam, T. Yildirim, A. B. Harris, A. Aharony, and O. Entin-Wohlman, Phys. Rev. B **56**, 260 (1997).
  - [21] D. Petitgrand, S. V. Maleyev, P. Bourges, and A. S. Ivanov, Phys. Rev. B **59**, 1079 (1999).